Observing the Moon at Microwave Frequencies Using a Large-Diameter Deep Space Network Antenna

David D. Morabito, *Member, IEEE*, William Imbriale, *Life Fellow, IEEE*, and Stephen Keihm

***Abstract*—The Moon radiates energy at infrared and microwave wavelengths, in addition to reflecting sunlight at optical wavelengths. As a result, an antenna pointed at or near the Moon will result in an increase in system operating noise temperature, which needs to be accounted for in RF telecommunications, radio science or radiometric link calculations. The NASA Deep Space Network (DSN) may use its large-diameter antennas in future lunar robotic or human missions, and thus it is important to understand the nature of this temperature increase as a function of observing frequency, lunar phase, and angular position of the antenna beam on the lunar disk. This paper reports on a comprehensive lunar noise temperature measurement campaign and associated theoretical treatment for a 34-m diameter Deep Space Network antenna observing an extended source such as the Moon. A set of measurements over a wide range of lunar phase angles was acquired at DSS-13, a 34-m diameter beam waveguide antenna (BWG) located at Goldstone, California at 2.3 GHz (S-band), 8.4 GHz (X-band) and 32 GHz (Ka-band). For validation purposes, independent predictions of noise temperature increase were derived using a physical optics characterization of the 34-m diameter antenna gain patterns and Apollo model-based brightness temperature maps of the Moon as input. The model-based predictions of noise temperature increase were compared with the measurements at all three frequencies. In addition, a methodology is presented that relates noise temperature increase due to the Moon to disk-centered or disk-averaged brightness temperature of the Moon at the microwave frequencies of interest. Comparisons were made between the measurements and models in the domain of lunar disk-centered and disk-averaged brightness temperatures. It is anticipated that the measurements and associated theoretical development will be useful in developing telecommunications strategies for future high-rate Ka-band communications where large diameter DSN antennas will be required.**

***Index Terms*—Antenna radiation patterns, microwave antennas, Moon, temperature measurement.**

I. Introduction

WHEN ONE VIEWS the Moon, the light reflected from the Sun takes on different distinct appearances as a function of lunar phase. The phase cycle from successive new Moons repeats with the synodic period of about 29.5 days. At wavelengths (λ) other than those of visible light, there is less reflected radiation so the emission is dominated by thermal noise. This noise is related to the Moon's surface and near-surface temperature, which in turn is related to the properties of the lunar surface material and received solar insolation. The level of lunar infrared emission is well correlated with the lunar phase cycle, as it originates from a very thin surface layer. However, at millimeter and centimeter wavelengths, the amount of this variation is much less than at infrared since the radio emission originates deeper within the lunar surface (upper $\sim$10 centimeters). The surface layers are heated by conduction and the variations with lunar phase in the radio also lag behind the lunar phase cycle of solar heating. Radio observations of the Moon's brightness temperature at microwave frequencies show a somewhat sinusoidal variation with lunar phase about a mean brightness temperature. For $\lambda < 5\ \mathrm{cm}$, the amplitude of this variation exhibits discernible wavelength dependence, and its phase is consistent with the lunar cycle of solar insolation, but delayed due to latent heating effects. For $\lambda > 5\ \mathrm{cm}$, the variation is small or nonexistent [1], [2].

Missions are now being considered to revisit the Moon with future human and robotic expeditions. The success of such missions will require very high data rates and a thorough understanding of all contributions in telecommunications link calculations. Among these contributions, the additional system noise temperature increase $(\Delta \mathrm{T_{op}})$ while pointing a large diameter antenna onto the disk of the moon must be characterized, either by modeling or by direct measurement. The potential of using the NASA Deep Space Network (DSN) 34-m diameter beam waveguide antennas to realize high data rates [3] merits investigating these lunar noise temperature increases for this class of antennas.

A previous paper [4], presented the system noise temperature increase measurements $(\Delta \mathrm{T_{op}})$ due to the Moon for use in future human and robotic lunar telecom link calculations. These measurements were acquired at DSS-13, a 34-m diameter beam waveguide antenna located at the NASA Deep Space Communications Complex (DSCC) at Goldstone, near Barstow, California. The $(\Delta \mathrm{T_{op}})$ measurements were performed pointing the antenna boresight at the center of the lunar disk (antenna beam moon-centered) and at the limb of the lunar disk (antenna beam moved one lunar radius off-center). These measurements were then referred relative to the background noise temperature when pointed at cold sky, by moving the antenna beam sufficiently away from the Moon. The on-minus-off disk-centered noise temperature measurements were independently validated using a physical optics (PO) characterization of the DSS-13 antenna [5]. The limb-centered measurements would be useful for links where the antenna beam is pointed at the lunar limb such

Manuscript received July 25, 2007; revised October 10, 2007. The research described in this paper was carried out at the Jet Propulsion Laboratory, California Institute of Technology, under a contract with the National Aeronautics and Space Administration.

The authors are with the Jet Propulsion Laboratory, California Institute of Technology, Pasadena CA 91125 USA (e-mail: ddm@godzilla.jpl.nasa.gov).

Digital Object Identifier 10.1109/TAP.2007.915471

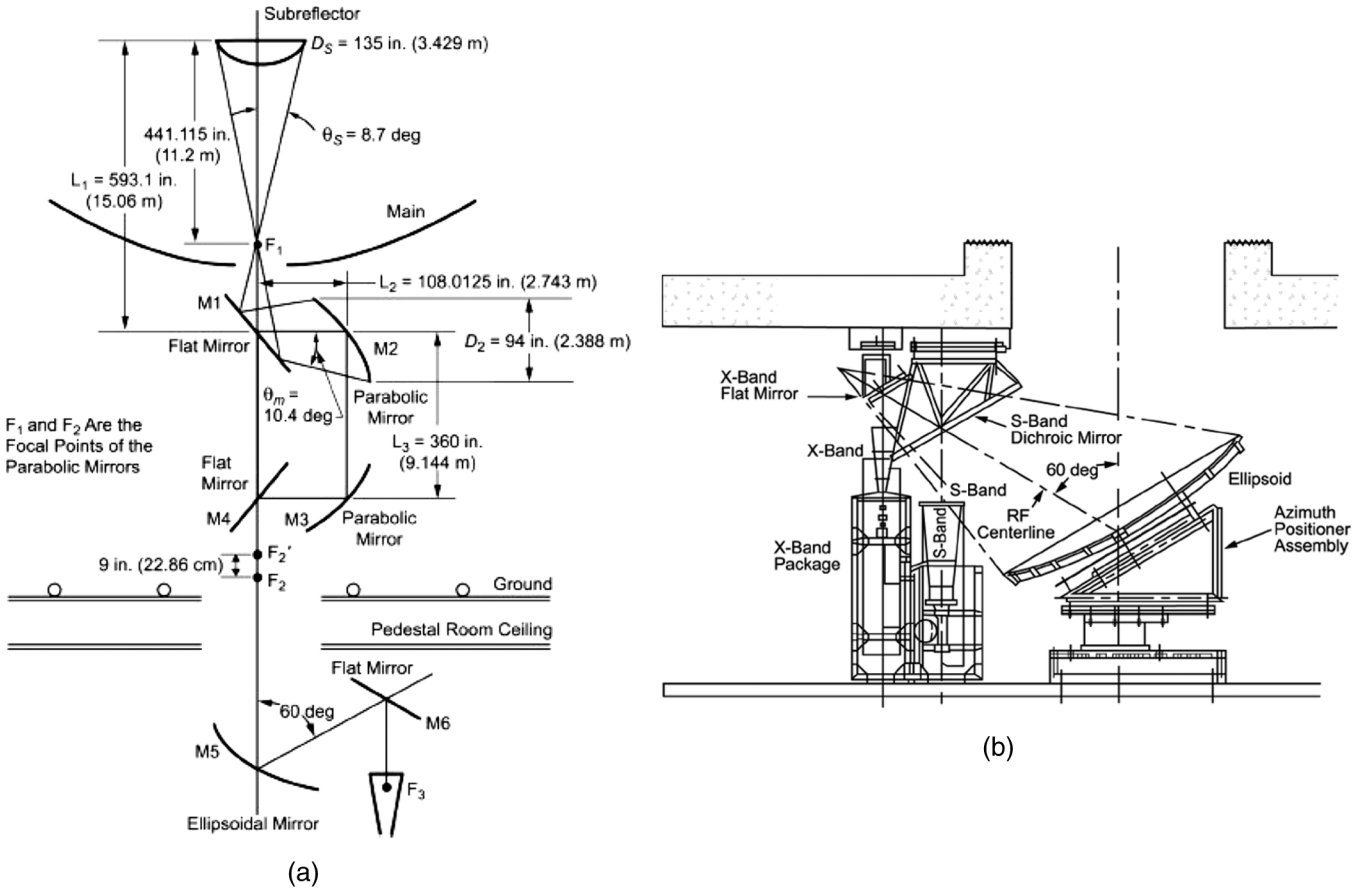

Fig. 1. DSS-13 Beam waveguide antenna S/X position. (a) Beam waveguide mirrors; (b) S/X feed arrangement.

as at Malapert Mountain near the lunar southern pole, a possible communications relay station site [6].

This paper reports on a comprehensive lunar noise temperature measurement campaign and associated theoretical treatment for a 34-m diameter DSN antenna used for deep-space communications observing an extended source, in the case of the Moon. A previous set of similar measurements performed in the 1970s at X-band made use of the 64-m diameter DSN antenna in Madrid, Spain (now a 70-m diameter antenna) [7], along with publication of subsequent maps of the full-moon [8]. The lunar noise temperature measurements [4] and supporting predictions from the PO analysis [5] will be combined in this paper and discussed in a coherent context with additional detail and elaboration.

II. Equipment Description and Calibrations

DSS-13 is a BWG antenna used for Research and Development activities in the DSN. This antenna is comprised of a 34-m diameter main reflector and a series of mirrors that guide the energy down into a subterranean pedestal room [see Fig. 1(a)]. There, a central ellipsoid mirror is used to guide the energy to one of several feed packages situated on a ring concentric with the antenna's azimuth axis. The use of a subterranean room insulates the equipment from outside weather effects such as rain and wind as well as facilitating equipment maintenance. Two of the feed packages utilized for this experiment were located at the S/X position (or feed station) making use of an S/X dichroic plate, a mirror, and S-band and X-band feed packages, consisting of feed horns, low noise amplifiers and follow-on equipment [see Fig. 1(b)]. The dichroic plate allows the higher frequency X-band radiation to pass through, guiding it to the X-band feed package (via another mirror), and reflects the lower frequency S-band radiation into the S-band feed package, thus allowing for simultaneous measurement of S-band and X-band noise temperatures.

The X/Ka station on the concentric ring makes use of an X/Ka dichroic plate, a mirror, and X-band and Ka-band packages (see Fig. 2), allowing for simultaneous measurement of X-band and Ka-band noise temperatures. The packages all include front-end amplifiers where high electron mobility transistors (HEMTs) are used as active elements. The equipment includes downconverters, follow-on microwave equipment, and calibration hardware (noise diodes and ambient loads). A total power radiometer (TPR) is used to measure the system noise temperature after the system is calibrated. The specifics of each observing wavelength are provided in Table I.

Prior to each measurement session a sequence of calibrations was performed to relate measured power to system operating noise temperature and to characterize system linearity [9]. Changes in gain measured over the calibration period (few minutes) usually lie below 0.1% (0.004 dB). During the lunar noise temperature measurement period of about 1 hour duration (following the calibration), the projected uncertainty due to gain variation is small (~1%), as the pedestal room environ-

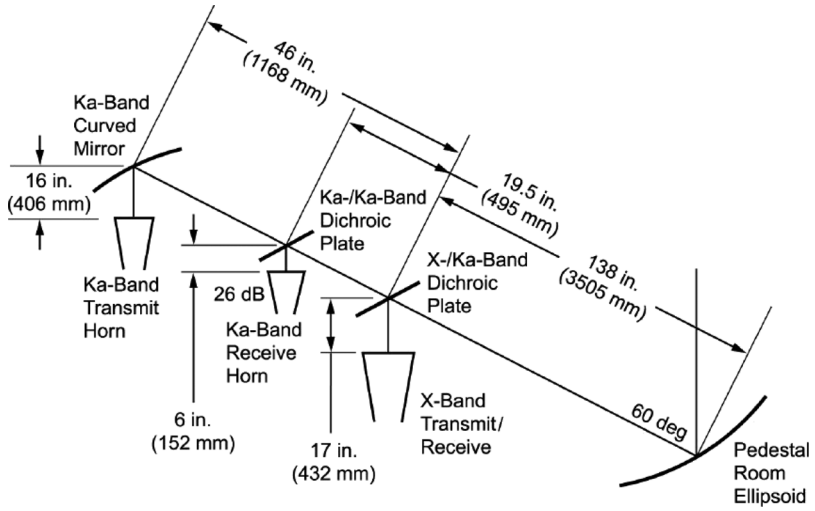

Fig. 2. X/Ka position dimensions and layout.

TABLE I
OBSERVING FREQUENCY SPECIFICATIONS

Band	Frequency (MHz)	Bandwidth (MHz)	Polarization	Feed Package
S	2295	20	LCP	S/X
X	8425	20	LCP	S/X
X	8415	20	LCP	X/Ka
Ka	32000	30	RCP	X/Ka

ment is well controlled and isolated from outside environmental changes. For additional details of the calibration see [4].

III. PHYSICAL OPTICS CHARACTERIZATION USING MODEL-GENERATED $\mathrm{T_B}$ MAPS

This section will discuss the use of physical optics (PO) theory for estimating the DSS-13 antenna gain patterns and predicting the increase in system noise temperature $(\Delta \mathrm{T_{op}})$ due to the Moon at the frequencies of interest, with Apollo-based model-generated brightness temperature $(\mathrm{T_B})$ maps of the Moon being the target source. The model $\mathrm{T_B}$ maps were computed from a detailed model of the depth- and temperature-dependent thermal and electrical properties of the lunar regolith (fragmentary debris of soil and rocks that cover the lunar surface). These properties were derived primarily from Apollo program results and are described in detail in [10]. Validation of the model, through comparisons with Earth-based Moon measurements at $\lambda \sim$0.1–20 cm, is described in [11]. The lunar $\mathrm{T_B}$ model has an estimated absolute accuracy of $\pm 3\%$ and has been used world-wide since the 1970's as a calibration source for both Earth-based and spacecraft antennas [12], [13].

The $\mathrm{T_B}$ maps were available at lunar phase angles ranging from 0° to 360° degrees in steps of 12°, (where 180° denotes full-Moon and 0° denotes new-Moon. Graphical examples of model $\mathrm{T_B}$ maps at Ka-band are presented in Fig. 3 where the differences between full Moon (3a) and new Moon (3b) are evident as well as the asymmetry in each map. Unlike previous antenna efficiency measurement campaigns where the radio source size was smaller than the main beam of the antenna [14], the Moon is an extended source whose apparent size ($\sim 0.52°$) is comparable to the null-to-null beamwidth of the 34-m diameter antenna main beam at S-band, and significantly larger than the angular span of the main beam and major sidelobes at X-band and Ka-band. For reference, the half-power beamwidths are 0.242° at S-band, 0.066° at X-band and 0.017° at Ka-band. A visual description of the S-band, X-band and Ka-band idealized beam slices against the backdrop of the lunar disk is provided in Fig. 4.

The physical optics (PO) analysis proceeds as follows: The antenna noise temperature increase (K) due to a source with brightness temperature $(\mathrm{T_B})$ distribution $\mathrm{T_B}(\theta,\phi)$ in spherical coordinates is given as [5], [15]

$$T_A = \frac{\int_0^{\pi}\int_0^{2\pi} P(\theta,\phi) T_b(\theta,\phi)\sin(\theta) d\phi d\theta}{\int_0^{\pi}\int_0^{2\pi} P(\theta,\phi)\sin(\theta) d\phi d\theta} \tag{1}$$

where $\mathrm{P}(\theta,\phi)$ is the power per unit solid angle relative to the peak of the antenna power pattern, θ is the radial (or polar) angle component in the sky relative to the beam center, and ϕ is the clock (or azimuthal) component.

Since the denominator in (1) is the total radiated power, $\mathrm{P_T}$, the antenna normalized gain $\mathrm{G}(\theta,\phi)$ can be expressed as

$$G(\theta,\phi) = 4\pi \frac{P(\theta,\phi)}{P_T}. \tag{2}$$

Substituting (2) into (1) yields

$$T_A = \frac{1}{4\pi}\int_0^{\pi}\int_0^{2\pi} G(\theta,\phi) T_B(\theta,\phi)\sin(\theta) d\phi d\theta. \tag{3}$$

To compute the noise temperature increase caused by the Moon, it is necessary to convolve the brightness temperature

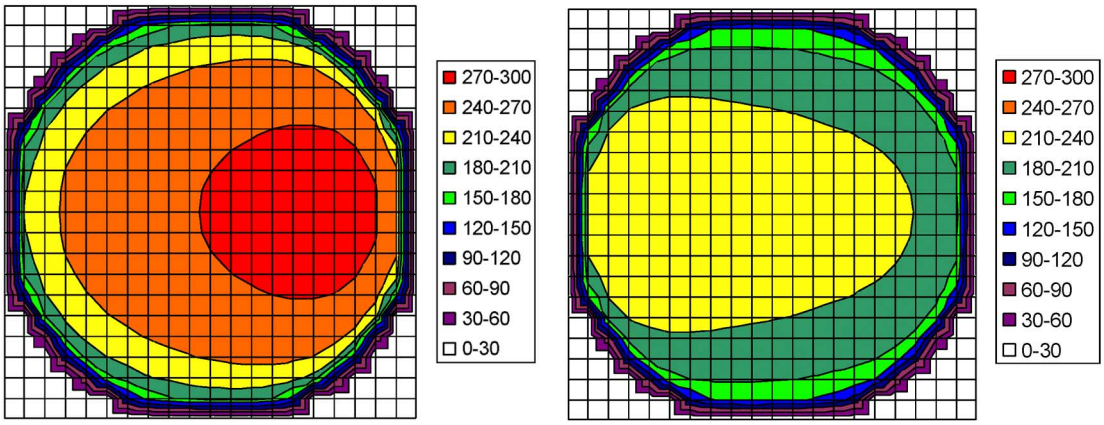

(a) (b)

Fig. 3. Ka-band brightness temperature maps at (a) Full Moon (180°) and (b) New Moon (0°). Units are Kelvins.

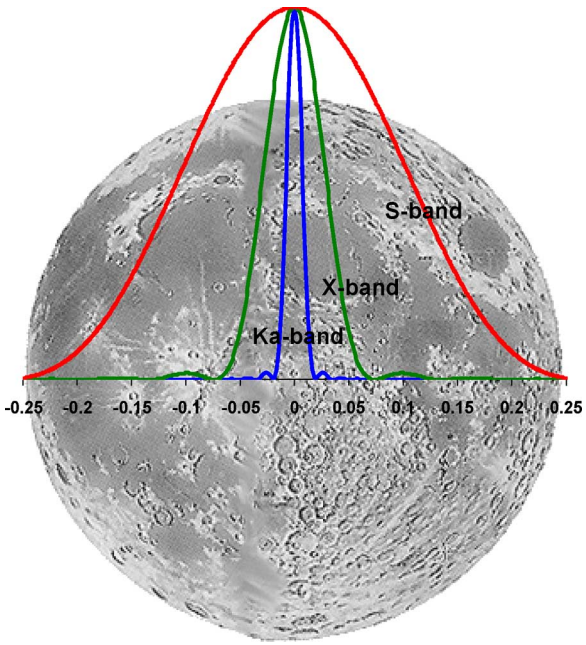

Fig. 4. Lunar disk with cross-sections of idealized antenna beam pattern slices for a 34-m diameter antenna at S-band (2295 MHz), X-band (8425 MHz) and Ka-band (32,000 MHz). Horizontal scale is in degrees from center of the Moon (approximate). (Moon image courtesy of NASA.)

distribution of the Moon with the antenna pattern over the extent of the lunar disk. The noise temperature increase is given by

$$T_A = \frac{1}{4\pi} \int_0^{\theta_m} \int_0^{2\pi} G(\theta,\phi) T_B(\theta,\phi) \sin(\theta) d\phi d\theta \qquad (4)$$

where the integration is performed over the angular area of the sky subtended by the Moon (polar angle limit of $\theta_{\rm m}$). Although the Moon's angular diameter as seen from the Earth changes (from 0.49° to 0.56°) due to the non-unity orbital eccentricity of the Moon, we use a single nominal value of 0.5° for this analysis. We have not yet accounted for atmospheric attenuation, non-PO losses between main reflector and feed, or lunar blockage of the cosmic background in (4).

We now discuss the determination of the gain pattern, $\mathrm{G}(\theta,\phi)$, for the DSS-13 antenna at the frequencies of interest. The geometry of the BWG antenna is described in [15]. The two configurations to be analyzed are the S- and X-band frequencies for the S/X band feed position and the X- and Ka-band frequencies for the X/Ka-band position. The geometry for the S/X band feed position equipment is shown in Fig. 1(b). This configuration is analyzed for the transmit mode and reciprocity is used for the received mode. Initially the pattern for the corrugated feed horn is computed using the horn geometry and mode matching software described in [15]. The horn pattern is used to determine the physical optics (PO) currents on the first mirror. The currents on the first mirror are then used to determine the currents on the second mirror as also described in [15]. The proper power normalization is utilized as all the power from the feed does not get to the second mirror as some of it spills past the first mirror. The procedure is repeated for each of the other mirrors, the subreflector, and the main reflector. The currents radiating from the main reflector are utilized to obtain $\mathrm{G}(\theta,\phi)$. For accuracy and completeness, the actual distorted shape of the main reflector, the subreflector and strut blocking pattern are required, as it significantly affects the patterns at X- and Ka-band. The blockage due to the subreflector and struts were determined from holography measurements on the DSS-13 antenna [16].

The measured holographic pattern in Fig. 5(a) was analyzed to evaluate blockage. The resulting blockage mask [see Fig. 5(b)] was applied to the main reflector current distribution (the PO currents are set to zero). Using the geometry from Fig. 1(b) and the strut mask of Fig. 5(b), the far field radiation pattern was computed at S-band (2.3 GHz) and is shown in Fig. 6 along with results of point source measurements. Cross-scans were performed on two different days using radio sources Virgo A and 3C405 in order to characterize actual antenna pattern slices out to ± 1.2 deg in two orthogonal directions, declination (DEC) and cross-declination (XDEC). On 2004/236, the elevation angle varied from 44° to 39° during the

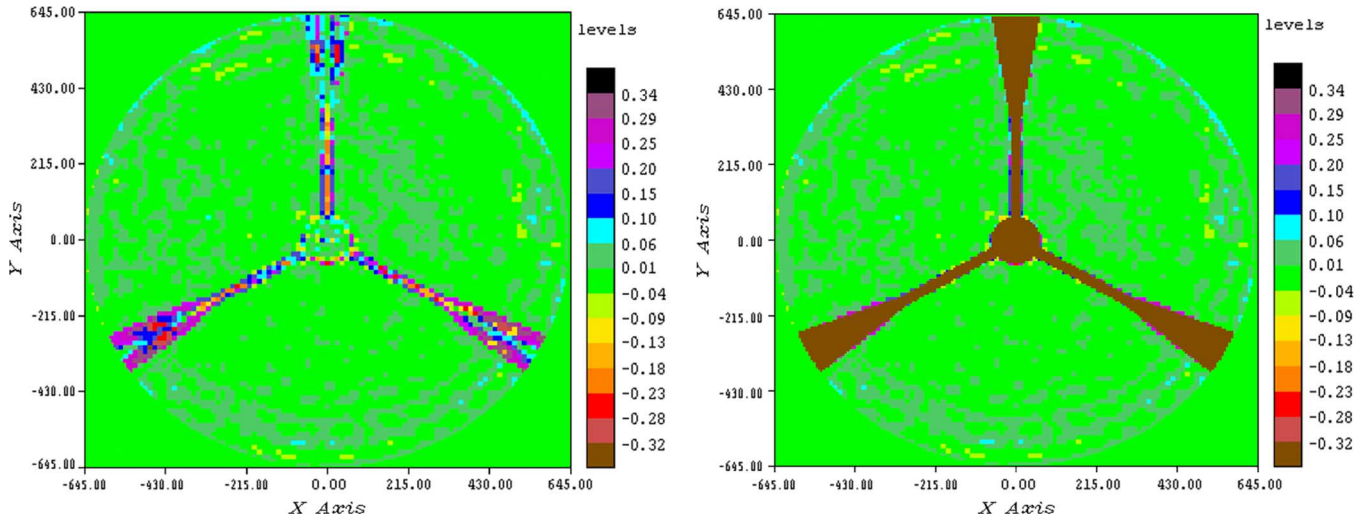

Fig. 5. (a) Holographic amplitude map of DSS-13 at rigging angle, (b) resulting masking used to model blockage from struts and subreflector [5].

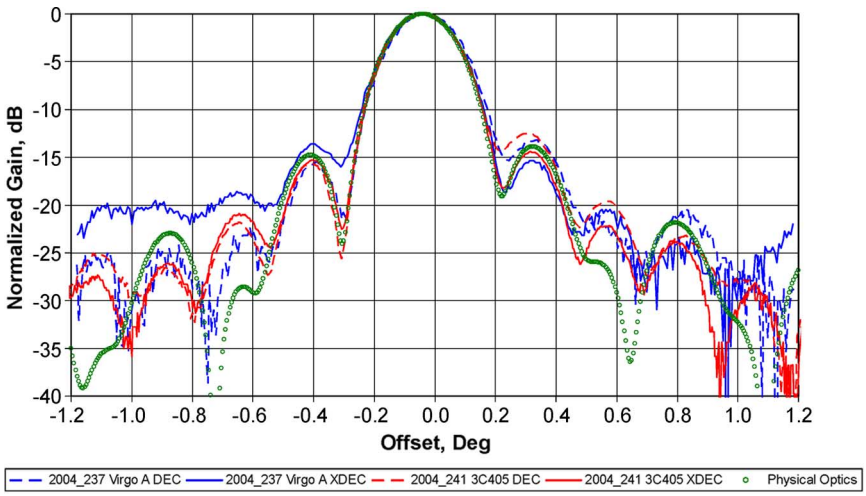

Fig. 6. S-band antenna pattern slices in two orthogonal directions as measured on 2004/236 in blue, using Virgo A (M87) and on 2004/241 in red, using 3C 405. Also shown is the physical optics derived RCP radiation pattern in green (offset by -0.04 deg).

cross-scan. On day 2004/241, the elevation angle varied from 70° to 75° during the cross-scan. There is significant asymmetry of the measured sidelobe pattern slices upon inspection of Fig. 6. The PO-derived antenna pattern in Fig. 6 is offset $-0.04°$ to provide for alignment with the measured pattern slices. There is reasonable agreement between the PO-derived pattern and the measured pattern, especially in the main lobe and first sidelobes. The difference in the patterns measured on the two different days is likely due to changing gravitational deformation of the structure with elevation angle.

Cross-scan measurements of the antenna pattern at X-band and Ka-band were also conducted using radio sources, but there was insufficient source flux to accurately resolve the weak sidelobe pattern detail. An X-band normalized gain pattern measurement was obtained by performing cross-scans on the MRO spacecraft during its early cruise [17] when it was close to the Earth providing a very strong received signal on October 20, 2005 (see Fig. 7). This pattern shows very good agreement in the main lobe and reasonable agreement in the sidelobes when compared with the PO derived pattern. The PO-derived antenna pattern at Ka-band is shown in Fig. 8. No independent measurements of the antenna pattern were available at Ka-band for comparison.

The PO-derived noise temperature increase, $\mathrm{T_A}$ in (4), is the temperature increase one would measure at the input plane of the feedhorn in a vacuum using the 34-m diameter antenna pointed at the center of the Moon. Several factors must be taken into account in order to relate this PO-derived noise temperature increase to "on-source" minus "off-source" noise temperature measurements $\Delta \mathrm{T_{op}}$. First, the effective contribution of the cosmic microwave background in the "off-source" system noise temperature measurements is assumed to not be present (or negligible) in the "on-source" lunar disk-centered measurements. In addition, other effects such as atmospheric attenuation, system non-linearity, and losses not considered by the PO analysis need to be estimated. The PO-derived noise temperature increase, $\mathrm{T_A}$

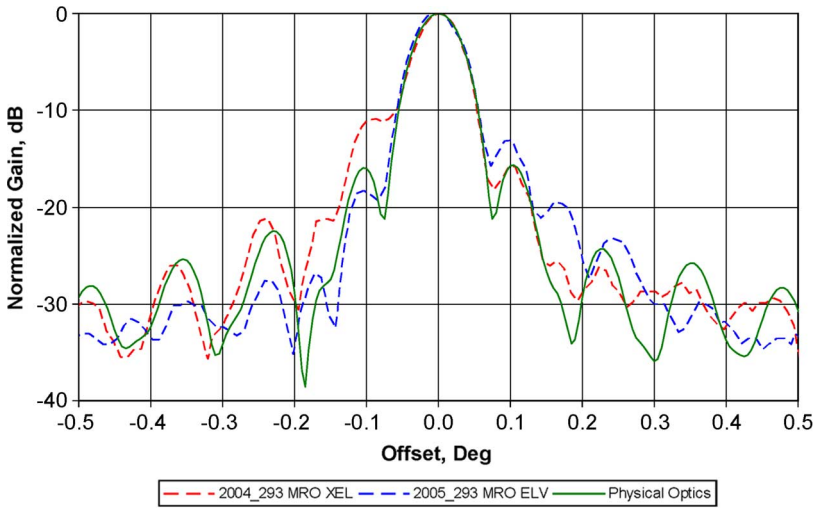

Fig. 7. X-band RCP radiation pattern measured by performing a cross-scan on the MRO spacecraft during early cruise on October 20, 2005 (2005/293): cross-elevation (red), elevation (blue) along with PO-derived pattern (green).

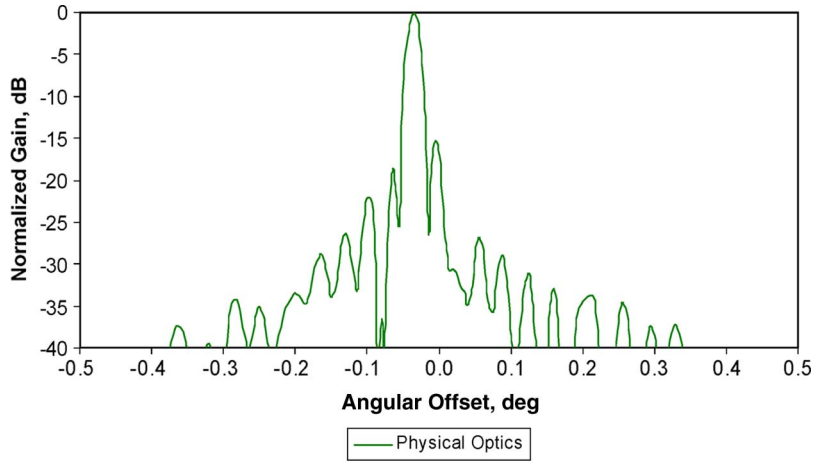

Fig. 8. Ka-band RCP normalized radiation pattern derived from PO analysis.

in (4), can be related to the raw ON-OFF system noise temperature measurement, $\Delta \mathrm{T_{op}}$, by

$$T_A = \Delta T_{\mathrm{op}} L_{\mathrm{atm}} L_{\mathrm{feed}} f + T_{\cos mic,e} \tag{5}$$

where $\mathrm{T_{cosmic,e}}$ is the effective amount of the cosmic background present in the off-source measurement but not in the disk-centered measurement, and is given by

$$T_{\cos mic,e} = \frac{\int_0^{\pi}\int_0^{\theta_m} P(\theta,\phi) T_{\cos mic}(\theta,\phi)\sin(\theta)d\phi d\theta}{\int_0^{\pi}\int_0^{2\pi} P(\theta,\phi)\sin(\theta)d\phi d\theta}. \tag{6}$$

The cosmic background is integrated over the angular extent of the Moon and we assume $\mathrm{T_{cosmic}}(\theta,\phi) = 2.725$ K for all (θ,ϕ). $\mathrm{L_{atm}}$ in (5) is the atmospheric loss factor, f corrects for any system non-linearity that may be present, and $\mathrm{L_{feed}}$ accounts for losses between the main reflector and LNA input that are not considered in the PO analysis.

The atmospheric loss factor is elevation angle dependent as well as frequency dependent. For nominal elevation angles above 20° in the Goldstone desert climate, $\mathrm{L_{atm}}$ is close to unity for S-band and X-band (typically 1.01) but can be significant for Ka-band depending on weather conditions and elevation angle (1.04 to 1.2). The atmospheric loss factor (defined here to be >1) as a function of elevation angle is given by

$$L_{\mathrm{atm}}(\theta) = e^{\tau(f)/\sin(\theta)} \tag{7}$$

where τ is the frequency-dependent optical depth of the atmosphere at zenith and θ is the elevation angle. The optical depth of the atmosphere can be estimated using a layered atmospheric model[1] with input values of pressure, temperature and relative humidity measurements obtained from sensors located near the antenna, or alternatively from on-site Water Vapor Radiometer sky brightness temperatures.

Once the PO analysis produces estimates of $\mathrm{T_A}$ using (4), one can obtain estimates of the effective PO efficiency using either

[1]S. Slobin, private communication.

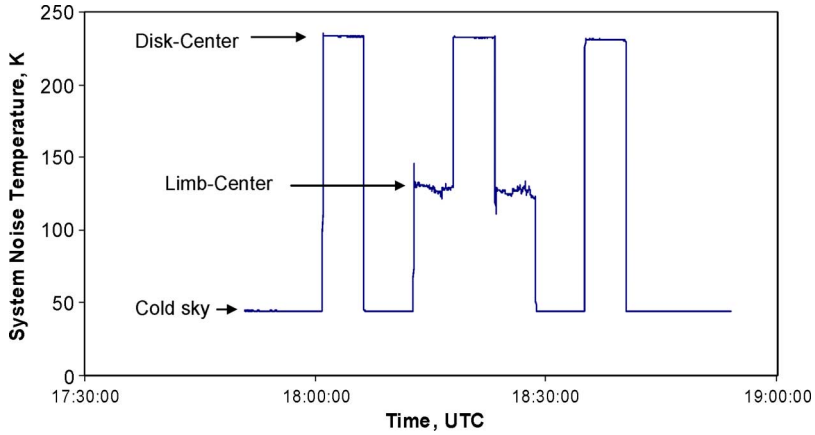

Fig. 9. Example of system noise temperature measurement sequence (X-band) taken on pass 2004/226 (August 13, 2004).

disk-averaged (S-band) or disk-centered (X-band and Ka-band) values of $\mathrm{T_B}$, defined by

$$\eta_{\mathrm{PO}} = \frac{T_A}{T_B}. \tag{8}$$

These PO-derived efficiencies can then be used to relate any raw measurements $\Delta \mathrm{T_{op}}$ to estimates of brightness temperature $\mathrm{T'_B}$ for comparison with the map values

$$T'_B = \frac{\Delta T_{\mathrm{op}} L_{\mathrm{atm}} L_{\mathrm{feed}} f + T_{\cos mic,e}}{\eta_{\mathrm{PO}}}. \tag{9}$$

In order to obtain a prediction of measured temperature increase, $\Delta \mathrm{T_{op}}$, we first compute a PO-derived gain pattern and then convolve it with the Moon maps to get a predicted PO noise temperature increase $\mathrm{T_A}$ using (4). This is then converted to a prediction of measured noise temperature increase by using a rearranged form of (5)

$$\Delta T_{\mathrm{op}} = \frac{T_A - T_{\cos mic,e}}{L_{\mathrm{atm}} L_{\mathrm{feed}} f}. \tag{10}$$

We can then compare the PO-derived predictions of noise temperature increase given by (10) with the raw measurements to be described in the next section.

IV. Comparison of Measurements and Predictions of Noise Temperature Increase

During 2004, a measurement campaign was conducted at DSS-13 in order to characterize the noise temperature increase $(\Delta \mathrm{T_{op}})$ one would see when using a 34-m diameter antenna pointed at the Moon, such as for future human and robotic missions. The measurement strategy assumes that the antenna main beam is comparable to or smaller than the source size, and thus would have to ensure off-source measurements (for baseline) were conducted sufficiently far enough away in both Moon-widths and antenna beamwidths to avoid noise pick-up of the Moon. On-source measurements include having the main beam boresight aligned at the center of the Moon. For the background reference noise temperature, the antenna is moved sufficiently far off-source in cross-elevation angle (direction parallel to the horizon) so as to minimize elevation angle dependent effects in the atmosphere. Appropriate filters at the input to the power meters of the TPR were used at each frequency (see Table I).

The noise temperature increase, $\Delta \mathrm{T_{op}}$, referenced to the center of the lunar disk [for comparison with PO-derived predictions in (10)] is given by

$$\Delta T_{\mathrm{op}}(\theta) = T_{\mathrm{disk-centered}}(\theta) - T_{\mathrm{off\_source}}(\theta) \tag{11}$$

where the disk-centered and off-source values are antenna temperature averages over the measurement period at the respective position.

The total system noise temperature was measured at several positions: the lunar disk center, the lunar limbs (offset $\sim 0.26^\circ$ in cross-elevation) and cold sky (offset $\sim 5^\circ$ for background) spending about 5-minutes in duration at each point. A lunar ephemeris was used at DSS-13 to track the specific points on the Moon (center and limbs). Because the measurement sequence is performed by alternatively repeating the on-source (disk-centered) and off-source (cold sky) positions, the temporal elevation angle dependence is effectively removed from the difference and therefore does not require corrective modeling in (11). An example of a sequence of measurements is provided in Fig. 9 for the case of X-band. Note that the limb-centered data exhibit the greatest visible fluctuations, whereas the disk-centered and cold sky measurements exhibit very little fluctuation. For examples of measurement sequences at other frequency bands and for detailed discussion on the limb-centered measurements, see [4].

The measurement sequence for the X/Ka feed position was conducted similarly to that for the S/X feed position but also included an additional boresight observation of an angularly nearby radio source to allow pointing offsets to be determined to better center the beam on the limb of the Moon during the limb-centered measurements. This is especially critical at Ka-band where the half-power beamwidth of the 34-m diameter antenna is $\sim$17 mdeg and the blind pointing model of DSS-13 near the ecliptic is accurate to $\sim$5 mdeg.

The resulting noise temperature measurements, $\Delta \mathrm{T_{op}}$, due to the Moon as a function of lunar phase angle are presented in Fig. 10. The average and standard deviation of this system

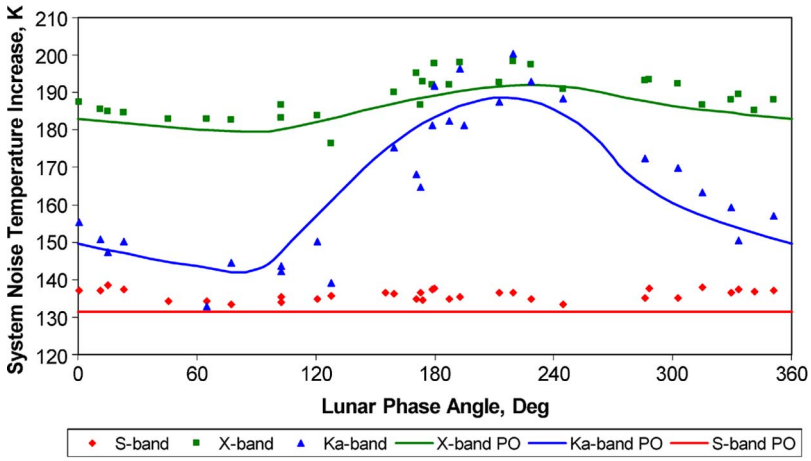

Fig. 10. ΔT_{op} measurements and PO-derived predictions for DSS-13 (beam centered on lunar disk) as a function of lunar phase (0°: new moon, 180°: full-moon). S-band disk-average (red); X-band disk-center (green); Ka-band disk-center (blue).

noise temperature difference due to the Moon provide information on its variability with lunar phase. The S-band ΔT_{op} (mean with standard deviation), 135.9 $\pm$ 1.4 K, exhibits very little variation about the mean, about 1% [4]. The X-band values, $\sim$ 189.1 $\pm$ 5.4 K, at the S/X package exhibits 2.8% variation. The Ka-band values, 165.7 $\pm$ 19.5 K, exhibits significantly more variation, 11.8%. It is interesting to note that the observed percent variation is virtually linear with radio frequency. Fig. 10 also shows the PO-derived curves referenced to nominal values of atmosphere attenuation, cosmic blockage, and any non-linearity (when applicable) using (10).

Polynomial fits of the data with the Moon-centered antenna beam have been performed [4] and allow for easy characterization of the noise temperature increase as a function of lunar phase for use in telecommunication link budgets. For link assets away from the lunar disk center, the noise temperature increase is expected to decrease to smaller values as the beam reaches the lunar limb. This is because the brightness temperature generally decreases away from the lunar center, and more of the beam begins to couple with the cold sky background, the degree of which depends on offset angle and frequency. The scatter of the data presented after removing the polynomial fit as a function of lunar phase is given in percent for the three frequencies about the mean values: S-band 1.0%, X-band 1.6% and Ka-band 3.6% [4].

A. S-Band Comparison

Carrying out the integration using the PO-derived S-band antenna pattern and S-band brightness temperature map (at any phase) into (4), an uncorrected noise temperature increase (T_A) of 136 K is computed for a disk-centered measurement at S-band. The effective PO-derived efficiency relating T_A and T_B can be computed using (4) after the results of the PO analysis are made available, where T_B is either an effective disk-averaged or disk-centered brightness temperature that can be obtained from the lunar brightness temperature maps. The effective PO-derived efficiency at S-band is about 61% for the case of the 34-m diameter antenna beam being disk-centered on the Moon assuming a disk-averaged S-band brightness temperature of 221.6 K for the Moon (using a pencil-beam convolution).

To translate T_A to predicted ΔT_{op}, we then take into consideration the additional contributions described in (10). For S-band, the atmosphere attenuation correction factor of 1.017 is determined from the average of the attenuation estimates over the measurement passes. The amount of the effective cosmic background $T_{cosmic,e}$ at S-band calculated using (6) and applied in (10) is 2.3 K. The resulting PO-predicted ΔT_{op} of 131.4 K from (10) compares reasonably well with the average of the ΔT_{op} measurements, 135.9 K, a 3% difference, as there is little variation with lunar phase (see Fig. 10). It should also be kept in mind that the correction for losses between the input plane of the feedhorn and input to the LNA, L_{feed} in (9), has not been applied, but is expected to be less than 2%.

B. X-Band Comparison

Measurements were made at X-band for both the S/X position and the X/Ka position [4]. However, from a theoretical design consideration, both designs are identical. Using the geometry shown in Fig. 1(b), the strut mask of Fig. 5(b), and the measured panel distortion at the rigging angle [16], the far field radiation pattern was computed as shown in Fig. 7. Carrying out the integration (4) using the derived PO pattern and X-band brightness temperature map (at 0° phase), a value for T_A of 189.1 K is computed for a disk-centered measurement at 0° lunar phase. The effective PO-derived efficiency at X-band $(\eta_{PO} = T_A/T_B)$ is thus about 79% for the case of the 34-m diameter antenna beam being disk-centered on the Moon assuming a disk-center X-band brightness temperature of 238.8 K for the Moon (from the center pixel of the lunar map at 0° phase).

After applying a cosmic background correction, $T_{cosmic,e}$ using (6), of 2.6 K and an atmospheric correction factor of 1.013, a prediction of 184.1 K results for the X-band ΔT_{op} using (10), comparing well with the ΔT_{op} measurement of 187.62 K ($\sim$2% error) at the 0° lunar phase angle. Note also the comparable amplitudes of the PO model-based and measured variations with lunar phase. It should also be kept in mind that the correction for losses between the input plane of the feedhorn

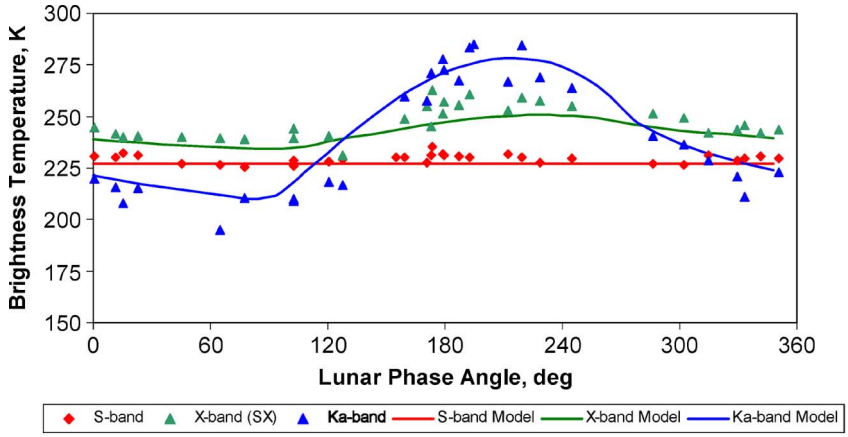

Fig. 11. $\mathrm{T_B}$ "Converted Measurements" (data points) and models (solid curves): S-band (disk-average), X-band (disk-center) and Ka-band (disk-center) versus lunar phase angle (180° = full Moon, 0° = new Moon).

and input to the LNA, $\mathrm{L_{feed}}$ in (9), has not been applied, but is expected to be less than 2%.

C. Ka-Band Comparison

The far field radiation pattern at Ka-band (32 GHz) (Fig. 8) was computed using the geometry shown in Fig. 2, the strut mask of Fig. 5(b) and the measured main reflector distortion at the rigging angle. An additional factor needs to be applied to the calculated pattern at Ka-band; the loss due to the RMS of the beam waveguide mirrors, which is significant at Ka-band. Assuming an average 3 mil (0.076 mm) RMS for each of the 6 mirrors,[2] the loss of an additional 7.06% of scattered power is needed to be taken into account. The resulting value for $\mathrm{T_A}$ extracted from convolving the antenna pattern with the model-generated Ka-band brightness temperature maps at 0° lunar phase was 165.9K using (4).

The effective PO-derived efficiency at Ka-band ($\eta_{\mathrm{PO}} = \mathrm{T_A}/\mathrm{T_B}$) is about 75% for the case of the 34-m diameter antenna beam being disk-centered on the Moon assuming a disk-center Ka-band brightness temperature of 221.5K for the Moon (from the center pixel of the lunar map at 0° phase). This PO-derived efficiency is virtually elevation angle independent. Comparing this with the 56% aperture efficiency for a point source at the rigging angle, we find that one big difference is that the loss due to main-reflector panel misalignment used for a point source is not applicable for the case of the Moon wherein the scattered energy caused by the panel misalignment is spread over the Moon and is therefore recovered on the disk of the Moon.

After applying an effective cosmic background correction ($\mathrm{T_{cosmic,e}}$) of 2.7 K, and an atmospheric attenuation factor of 1.06 (at the 0° phase angle of the measurement pass), the resulting prediction for $\Delta\mathrm{T_{op}}$ of 154.0 K using (10) compares well with the measurement of 155.5K (a 1% error) acquired on day 2004/258 near the 0° lunar phase angle. Note also the agreement in amplitude and phase between the PO-modeled and measured lunation variations. The Ka-band $\Delta\mathrm{T_{op}}$ prediction curve depicted in Fig. 10 was calculated using (7) with a value for the atmosphere attenuation factor, $\mathrm{L_{atm}}$, of 1.09 computed from the average of the individual values of $\mathrm{L_{atm}}$ over all of the measurement sessions. It should also be kept in mind that the correction for losses between the input plane of the feedhorn and input to the LNA, $\mathrm{L_{feed}}$ in (9), has not been applied, but is expected to be less than 2%.

The effect of the distortion as a function of elevation at Ka-band was also examined. Using the measured holography maps of the distortion, computations were made for noise temperature difference for the range of elevation angles covering 5° to 85° at a lunar phase angle of 180° (full Moon). It was found that even though there is a significant variation in peak gain, the energy is redistributed over the angular extent of the Moon and thus has minimal effect on the measured noise temperature difference for the case of an extended source [5]. The Ka-band aperture efficiency over the extended lunar disk is virtually elevation angle independent. As the antenna elevation angle changes, the net power collected from the lunar disk does not change in the manner that it does for a point source, where the antenna is optimized for peak gain at the rigging angle.

V. Lunar Brightness Temperature Conversion and Comparisons

In order to better assess the consistency and precision of the noise temperature increase measurements, $\Delta\mathrm{T_{op}}$, these were converted to brightness temperature $\mathrm{T_B}$ and then compared with the Apollo model-based $\mathrm{T_B}$ values as a function of lunar phase. The conversion from $\Delta\mathrm{T_{op}}$ to $\mathrm{T_A}$ was performed by first applying the corrections described in (5) for each pass. Then $\mathrm{T_A}$ was converted to $\mathrm{T_B}$ using the efficiencies derived from the PO analysis using (9). Fig. 11 summarizes these disk-centered lunar brightness temperature "measurements" (data points) along with the Apollo-based $\mathrm{T_B}$ models (solid curves) extracted from the maps that one would see within the main beam of the antenna, as a function of lunar phase angle. The S-band model in Fig. 11 is disk-averaged over the main beam. The X-band and Ka-band models in Fig. 11 are disk-centered (effectively the $\mathrm{T_B}$ map center pixel values).

[2]Britcliffe, M., private communication, Jet Propulsion Laboratory, Pasadena, California, 2007.

Much of the scatter of the data points about the model curves in Fig. 11 is likely attributed to errors in atmospheric modeling, pointing uncertainties, and libration effects that are not accounted for in the ephemeris model used to point the antenna at the lunar center.

A systematic signature of brightness temperature versus lunar phase in Fig. 11 is clearly seen in the X-band and Ka-band measurements centered about 230 K to 240 K, while the disk-averaged S-band values centered near 227 K exhibit very little variation or signature. The amplitude of the lunar phase variation signature is larger for the shorter wavelength Ka-band than X-band as expected. The T_B measurements in Fig. 11 at each frequency track their respective models very well. It is reasonable to assume that the higher X-band and Ka-band average temperatures are expected for the smaller main beam which picks up mostly energy emanating from the disk center region, and does not pick up as much thermal emission from the lower emissivity regions nearer the limbs. However, because the main beam covers the entire Moon at S-band, it picks up more of the lower amount of emission nearer the limb, and thus reduces the average of the received S-band signal.

A. S-Band Comparison

From Fig. 11, one can see that there is little or no variation with lunar phase at S-band as is evident from the 1.0% measurement scatter about the mean. The correction of individual atmospheric loss factors for each pass did not significantly reduce the scatter in T_B relative to the comparable case of the raw measurements in Fig. 10.

B. X-Band Comparison

The X-band noise temperature increase measurements display a clearly systematic variation with lunar phase (Fig. 10) and the measurements converted to brightness temperature follow the T_B model quite well (Fig. 11). The X-band model in Fig. 11 takes the disk-centered pixel value from each T_B map at each lunar phase [10], and is consistent with other measurements at similar wavelengths [2]. There appears to be increased scatter of the data about the model around full Moon than at other lunar phase angles. The average of T_B over the data (over the sampled lunar phase angles) is 247 K, versus the 242 K average of the Apollo model values. The RMS scatter of the data points about the solid curve model is about 4K (or 2%), after the 5K bias is removed.

C. Ka-Band Comparison

Fig. 11 also displays the Ka-band brightness temperature measurements converted from the raw measurements using (9) (in blue) along with the brightness temperature model (from disk centered pixel for each map at each lunar phase in solid blue). The Ka-band Apollo-derived brightness temperature model and its variation with lunar phase have been found to be consistent with other measurements at similar wavelengths [2], [18], [19], and is of complex signature, a clear deviation from a pure sinusoid. Note that the agreement between model and measurements is extraordinary. The scatter in the Ka-band measurements about the model in Fig. 11 is about 10K (4%) and may include contributions from unmodeled libration effects (not corrected in the antenna pointing ephemeris used at the station) from the lunar center, or in uncertainties in the weather attenuation model. It is suspected that some of the Ka-band measurement outliers that lie below the model may have suffered additional atmospheric attenuation than what the model for Latm predicts using surface meteorological measurements at input. After applying a bias correction of 5K to the data points, the random scatter about the model is about 7.4K (3%).

VI. Conclusion

A physical optics characterization of the predicted noise temperature increase as a function of lunar phase for a 34-m diameter antenna pointed at the center of the Moon was presented for three deep-space frequency bands. The DSN deep-space frequencies include cases where the antenna beam-width is comparable to the Moon diameter (S-band), and where the beam-width is a small fraction of the Moon diameter (X-band and Ka-band). The noise-temperature increase predictions were then compared to a set of measurements acquired in 2004 at DSS-13 in Goldstone, California. The noise-temperature increase predictions and measurements were in agreement to within 4%, comparable to the estimated absolute accuracy of the lunar model brightness temperatures used as the prediction source. The noise temperature increase measurements were also converted to brightness temperatures, using beam efficiency estimates based on the physical optics analysis, to check for consistency and assess precision. These values of brightness temperature compared well with the Apollo model T_B values, both in lunation average and phase variations. This paper reports on the first comprehensive analysis of observing an extended source using a large diameter DSN antenna at microwave frequencies, where the treatment differs significantly from that of the usual case of a point source.

Acknowledgment

The expertise and comments of several people are very much appreciated including C. Naudet, W. Veruttipong, C. Stelzried, S. Slobin, and A. Kantak. The support of Y. Shen, R. Cesarone, R. Hastrup, G. Noreen and P. Estabrook is very much appreciated. The support of the DSS-13 Station Crew is also appreciated, especially R. Littlefair for his well appreciated efforts in developing and using automated script files to run the antenna during the data acquisition tracks.

References

[1] J. Kraus, *Radio Astronomy*. New York: McGraw-Hill, 1966.

[2] D. O. Muhleman, "Microwave emission from the moon," in *Thermal Characteristics of the Moon*, J. W. Lucas, Ed. Cambridge, MA: MIT Press, 1972, vol. 28, Progress in Astronautics and Aeronautics.

[3] G. Noreen, R. Cesarone, L. Deutsch, C. Edwards, T. Ely, B. Cook, D. Morabito, H. Hemmati, S. Piazzolla, R. Hastrup, D. Abraham, M. Sue, and F. Manshadi, "Integrated network architecture for sustained human and robotic exploration," in *Proc. IEEE Aerospace Conf.*, Big Sky, MT, Mar. 2005, pp. 1266–1285.

[4] D. D. Morabito, "Lunar noise temperature increase measurements at S-band, X-band and Ka-band using a 34-m diameter beam waveguide antenna," Jet Propulsion Laboratory, Pasadena, CA, The InterPlanetary Network Progress Rep. 42-166, Aug. 15, 2006.

[5] W. Imbriale, "Computing the noise temperature increase caused by pointing DSS 13 at the center of the moon," Jet Propulsion Laboratory, Pasadena, CA, The InterPlanetary Network Progress Rep. 42-166, Aug. 15, 2006.

[6] B. L. Sharpe and D. G. Schrunk, "Malapert mountain: Gateway to the moon," *Adv. Space Res.*, vol. 31, no. 11, pp. 2467–2472, 2003.
[7] B. Gary and S. Keihm, "Interpretation of ground-based microwave measurements of the moon using a detailed regolith properties model," in *Proc. 9th Lunar Sci. Conf.* , 1978, pp. 2885–2900.
[8] S. Keihm and B. Gary, "Comparison of theoretical and observed 3.55 cm brightness temperature maps of the full moon," in *Proc. 10th Lunar Sci. Conf.*, 1979, pp. 2311–2319.
[9] C. Stelzried and M. Klein, "Precision DSN radiometer systems: Impact on microwave calibrations," *Proc. IEEE*, vol. 82, pp. 776–787, May 1994.
[10] S. J. Keihm, "Interpretation of the lunar microwave brightness temperature spectrum: Feasibility of orbital heat flow mapping," in *Icarus 60*, 1984, pp. 568–589.
[11] S. J. Keihm and M. G. Langseth, "Lunar microwave brightness temperature observations reevaluated in the light of Apollo program findings," in *Icarus*, 1975, vol. 24, pp. 211–230.
[12] C. L. Bennett, G. F. Smoot, M. A. Janssen, S. Gulkis, A. Kogut, G. Hinshaw, C. Backus, M. G. Hauser, J. C. Mather, L. Rokke, L. Tenorio, D. T. Wilkinson, E. L. Wright, J. Aymon, G. DeAmici, N. W. Boggess, E. S. Cheng, P. D. Jackson, P. Keegstra, T. Kelsall, R. Kummerer, C. Lineweaver, P. M. Lubin, S. S. Meyer, S. H. Moseley, Jr., T. L. Murdock, J. Santana, R. A. Shafer, R. F. Silverberg, and R. Weiss, "COBE differential microwave radiometers (DMR): Calibration techniques," *Ap. J.*, vol. 391, pp. 466–482, 1992.
[13] R. E. Cofield, "Field-of-view calibration of the microwave limb sounder on the upper atmosphere research satellite," in *Proc. IEEE Int. Geoscience and Remote Sensing Symp. (IGARSS'94)*, Aug. 1994, vol. 4, pp. 2224–2227.
[14] D. D. Morabito, "The characterization of a 34-meter beam-waveguide antenna at Ka-band (32 GHz) and X-band (8.4 GHz)," *IEEE Antennas Propag. Mag.*, vol. 41, no. 4, pp. 23–34, August 1999.
[15] W. Imbriale, *Large Antennas of the Deep Space Network*. Hoboken, NJ: Wiley-Interscience, 2003.
[16] D. J. Rochblatt and B. L. Seidel, "Performance improvement of DSS-13 34-meter beam-waveguide antenna using the JPL microwave holography methodology," Jet Propulsion Laboratory, Pasadena, CA, The Telecommunications and Data Acquisition Progress Rep. 42-108, Oct. –Dec. 1991, Feb. 15, 1992, pp. 253–270.
[17] D. D. Morabito, D. Lee, M. M. Franco, and S. Shambayati, "Measurement of Mars reconnaissance orbiter equivalent isotropic radiated power during early cruise," Jet Propulsion Laboratory, Pasadena, CA, The InterPlanetary Network Progress Rep. 42-168, Feb. 15, 2007, pp. 1–19.
[18] R. Dicke and R. Beringer, "Microwave radiation from the sun and moon," *Astrophys. J.*, vol. 103, 1946.
[19] J. Piddington and H. Minnett, "Microwave thermal radiation from the moon," *Australian J. Sci. Res.*, ser. A2, Mar. 1949.

David D. Morabito (M'80) was born in Los Angeles, CA. Since 1973, he has worked at Caltech's Jet Propulsion Laboratory, Pasadena, CA, on several engineering and scientific research projects. Among the areas he has worked on are spacecraft navigation, Very Long Baseline Interferometry (VLBI), Radio Science experiments on the Voyager 2, Ulysses, and Galileo spacecraft, performance characterization of beam-waveguide antennas, media propagation effects on spacecraft telecommunication links, and telecommunications systems design for proposed future space missions. His most recent project is studying the use of Ka-band (32 GHz) for deep-space navigation and for spacecraft telecommunications. He has over 100 publications in several professional journals, and conference proceedings.

Dr. Morabito is a member of the American Astronomical Society and the American Geophysical Union.

William A. Imbriale (S'64–M'70–SM'91–F'93–LF'08) received the B.S. degree in engineering physics from Rutgers University, New Brunswick, NJ, in 1964, the M.S. degree in electrical engineering from the University of California, Los Angeles, in 1966, and the Ph.D. degree from the University of Illinois, Urbana-Champaign, in 1969.

He is a Senior Research Scientist in the Communications Ground System Section at the Jet Propulsion Laboratory (JPL) in Pasadena, CA. Since starting at JPL in 1980, he has led many advanced technology developments for large ground-station antennas, lightweight spacecraft antennas, and millimeter-wave spacecraft instruments. He is currently working on a technology contract for the Earth Sciences Technology Office (ESTO) to develop a subreflector consisting of MEMS switches integrated with patch reflect array elements that will compensate, in real time, for on-orbit distortions of a membrane inflatable antenna. He is also the lead engineer for the Spanish supplied High Gain Antenna System for the Mars Science Laboratory (MSL) rover. Earlier positions at JPL have included being the Assistant Manager for Microwaves in the Ground Antennas and Facilities Engineering Section and the Manager of the Radio Frequency and Microwave Subsystem Section. Prior to joining JPL in 1980, he was employed at the TRW Defense and Space Systems Group where he was the Subproject Manager for the Antennas of the TDRSS program. He has published extensively and has won three best paper awards.

Dr. Imbriale is a Life Fellow of the IEEE and has received numerous NASA honor awards, including the Exceptional Service Medal. From 1993 through 1995, he was a distinguished lecturer for the Antennas and Propagation Society, speaking on beam-waveguide antennas and the evolution of the Deep Space Network antennas. He was a member of the Administration Committee of the IEEE Antennas and Propagation Society and general chairman of the 1995 International IEEE Antennas and Propagation International Symposium, held in Newport Beach, California. He has lectured and taught engineering courses at several learning institutions, including the University of California, Los Angeles and the University of Southern California. He is also a consultant to industry on all aspects of antenna analysis and design.

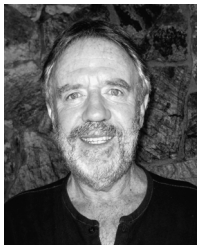

Stephen Keihm received the B.S. degree in Physics from Fordham University, Bronx, NY, in 1968, the B.S. degree in mechanical engineering from Columbia University, New York, in 1969, and the M.S. degree in astronautical science from Stanford University, Stanford, CA, in 1970.

From 1970 to 1978, he worked as a Research Assistant, then Staff Associate at the Lamont-Doherty Geological Observatory of Columbia University. While at Lamont, he served as Co-Investigator for the Apollo 15 and 17 lunar heat flow experiments, and Principal Investigator in studies of the thermal and electrical properties of the lunar regolith. In 1978, he joined the Planetary Science Institute, Pasadena, CA, where he conducted theoretical studies for the interpretation of data from the remote sensing of planetary surfaces. Since 1982, he has worked at the Jet Propulsion Laboratory, California Institute of Technology, Pasadena. At JPL, he has developed lunar calibration models for the Cosmic Background Explorer (COBE) Experiment, the Microwave Limb Sounder (MLS) instrument, and Rosetta Microwave Radiometer (MIRO) instrument. He has also worked extensively in the areas of algorithm development and data interpretation for earth-based, aircraft, and satellite microwave measurements of the atmosphere and sea surface. Currently, he is Instrument Scientist for the Cassini Radio Science Tropospheric Calibration System and Supervisor of the Ground-Based Microwave Applications Group at JPL.